frontiers in Remote Sensing

TYPE Original Research
PUBLISHED 24 July 2026
DOI 10.3389/frsen.2026.1856867

Check for updates

OPEN ACCESS

EDITED BY
Zhigang Cao,
Chinese Academy of Sciences (CAS), China

REVIEWED BY
Yulong Guo,
Henan Agricultural University, China
Jiahan Xv,
Northwest University, China

*CORRESPONDENCE
Valeria La Pegna,
valeria.la.pegna@uniroma2.it

RECEIVED 15 April 2026
REVISED 16 June 2026
ACCEPTED 29 June 2026
PUBLISHED 24 July 2026

CITATION
La Pegna V, Seo S, De Santis D, Del Frate F and Loyola D (2026) Comparative analysis on spectral characteristics of PRISMA and EnMAP hyperspectral missions. *Front. Remote Sens.* 7:1856867. doi: 10.3389/frsen.2026.1856867

COPYRIGHT
© 2026 La Pegna, Seo, De Santis, Del Frate and Loyola. This is an open-access article distributed under the terms of the Creative Commons Attribution License (CC BY). The use, distribution or reproduction in other forums is permitted, provided the original author(s) and the copyright owner(s) are credited and that the original publication in this journal is cited, in accordance with accepted academic practice. No use, distribution or reproduction is permitted which does not comply with these terms.

Comparative analysis on spectral characteristics of PRISMA and EnMAP hyperspectral missions

Valeria La Pegna[1,2]*, Sora Seo[3], Davide De Santis[1,2], Fabio Del Frate[1] and Diego Loyola[3]

[1]Earth Observation Laboratory, Department of Civil Engineering and Computer Engineering (DICII), University of Rome Tor Vergata, Rome, Italy, [2]Blue Dot Observation Srl, Rome, Italy, [3]Institut für Methodik der Fernerkundung (IMF), Deutsches Zentrum für Luft und Raumfahrt (DLR), Weßling, Germany

Given the similarities in their instrumental characteristics, a comparative analysis was conducted between hyperspectral missions of PRISMA, operated by the Italian Space Agency (ASI), and EnMAP, developed by the German Aerospace Center (DLR). This work investigates both the similarities and discrepancies between these two satellite optical data, providing an outline of the spectral regions where data from both sensors can be reliably interchanged. The analysis was performed by analyzing the full visible and near-infrared (VNIR) spectrum and by examining selected spectral ranges sensitive to key environmental parameters, such as nitrogen dioxide, chlorophyll and NDVI. A total of 11 PRISMA and EnMAP co-located hyperspectral image pairs acquired across different seasons over the Euro-Mediterranean region were analyzed, focusing on representative land cover classes (bare soil, vegetation, urban areas and waters). Preprocessing steps were applied to standardize the acquisition viewing geometries, and the top of atmosphere (TOA) level of products from the two sensors were used to avoid inconsistencies introduced by atmospheric correction schemes adopted by each operating agency. Overall, the quantitative and qualitative assessments confirm a strong correspondence between the PRISMA and EnMAP hyperspectral measurements across the VNIR spectrum, with SAM always below 0.1 rad. However, the statistical analysis reveals relatively low consistency between the two sensors for the vegetation sensitive spectral window (750–940 nm), where larger deviations are observed with STD of 0.067 and SAM of 0.097, while the NO_2 spectral range (420–500 nm) shows lower SAM of 0.048 and STD of 0.045.

KEYWORDS
EnMAP, hyperspectral imagery, PRISMA, remote sensing, spectral comparison

1 Introduction

Over the last decades, hyperspectral remote sensing has become increasingly important for environmental monitoring due to its ability to detect subtle spectral signatures with high precision. By providing detailed spectral information, hyperspectral observations enable accurate material identification and quantitative assessment, thereby supporting effective management of natural resources (Rajabi et al., 2024). Hyperspectral sensors acquire data across hundreds of contiguous, narrow spectral bands, capturing variations in the interaction between surface materials and electromagnetic radiation in accordance with the principles of spectral analysis (Zdravcheva, 2019).

In the field of optical earth observations, hyperspectral instruments offer continuous spectral coverage without gaps, enabling a comprehensive representation of environmental features from the perspective of electromagnetic radiation (Stuart et al., 2019). The

contiguous spectral content derives a large variety of applications in remote sensing across different environmental sectors, including atmospheric trace gas retrieval, agriculture and soil monitoring, and the characterization of inland and coastal waters (Cheng et al., 2025). Furthermore, hyperspectral mission datasets bridge the gap between localized field observations and the coarser spectral sampling of multispectral satellite observations, facilitating the integration of multi-scale datasets (Stuart et al., 2019).

The earliest hyperspectral observations were conducted from airborne platforms (Calin et al., 2021). Since 1987, the Airborne Visible/Infrared Imaging Spectrometer (AVIRIS) instrument, developed by Jet Propulsion Laboratory (JPL), has been deployed on various aircraft, acquiring adjacent images in 224 spectral channels (Green et al., 1998). Other airborne programs equipped with hyperspectral cameras, such as HyMap (Kruse et al., 2000), DLR HySpex (Baumgartner et al., 2012) and ESA-APEX (Schaepman et al., 2015), have demonstrated the importance of using high resolution spectral information. Spaceborne hyperspectral missions soon followed, starting with the Hyperion Imaging Spectrometer aboard EO-1 satellite, launched in early 2000by NASA (Pearlman et al., 2003). Since then, technological advancements have enabled the installation of hyperspectral cameras on satellite platforms, resulting in a series of missions, including DESIS by DLR launched in 2018 (Krutz et al., 2019); Gaofen-5 by the CHEOS launched in 2018 (Liu et al., 2019); HySIS by ISRO launched in 2018 (Mahalingam et al., 2019); PRISMA by ASI launched in 2019 (Candela et al., 2016); HISUI by METI launched in 2019 (Iwasaki et al., 2011); EnMAP by DLR launched in 2022 (Kaufmann et al., 2005) and EMIT by NASA launched in 2022 (Green, 2022). Also significant to mention is the near future of hyperspectral missions, such as ESA's CHIME satellite, scheduled for launch in 2028, which will expand the actual Copernicus constellation, ensuring high spectral resolution and 11 days of revisit time (Nieke et al., 2023). The main advantage of using hyperspectral imaging sensors on spaceborne instruments still stays in the consistency of acquisition properties, relying on acquisition angles, constant georeferencing and repeated revisit time. In addition, these sensors can also support more sophisticated spectral-spatial models, resulting in more accurate image segmentation and classification (Qian, 2022) and improving performances in parameters predictions, providing in this way an important advantage for optical satellite analysis, if compared with multispectral sensor alternatives (Zandler et al., 2015).

This study focuses on two hyperspectral satellite missions, PRISMA (PRecursore IperSpettrale della Missione Applicativa) and EnMAP (Environmental Mapping and Analysis Program), which present comparable designs in terms of spatial and spectral resolutions (Caporusso et al., 2020; Carmona et al., 2024). Their technical similarities make them suitable for analogous applications and facilitate synergistic analyses. The PRISMA mission is a precursor designed for optical Earth observation and innovative environmental monitoring, developed by Italian Space Agency (ASI) and released in 2019. The mission acquires and delivers hyperspectral and panchromatic images to support a variety of remote sensing applications, including resource management, environmental monitoring, and disaster management (Loizzo et al., 2018). Similarly, the EnMAP mission, managed by the German Aerospace Agency (DLR) and launched in 2022, builds upon the scientific and technological heritage of the DESIS mission (Habermeyer et al., 2024). EnMAP supports a wide variety of applications in agriculture, forestry, water quality management, and geology by enabling detailed monitoring, characterization, and parameter extraction for vegetation, soil, and inland and coastal waters on a global scale (Stuffler et al., 2009). Both missions aim to provide high spatial and spectral resolution data with consistent temporal coverage to support a wide range of environmental applications. Given their overlapping operational objectives and characteristics, evaluating the potential complementarity of these two sensors requires a rigorous analysis of their spectral characteristics to identify cross-sensor consistencies and systematic offsets.

Despite this potential, only a limited number of studies have evaluated the consistency between the hyperspectral imagery provided by these two sensors (Canero et al., 2024). Existing assessments are mainly constrained by localized validation using *in situ* measurements collected during dedicated field campaigns (Musacchio et al., 2024; Rasooli et al., 2024). While such studies demonstrate the quality of individual sensor products, they do not fully account for the variations encountered across different biomes and atmospheric conditions. Consequently, comprehensive satellite-based intercomparison is essential to better understand the collective exploitation of the PRISMA and EnMAP missions for global environmental monitoring.

To assess the functional operability of the data from these two sensors, evaluations also over specific environmental sensitivity domains were performed where the interoperability of the two hyperspectral cubes can represent an interesting aspect. Specifically, atmospheric nitrogen dioxide (NO_2) was selected being a valuable parameter, given its established significance in air quality monitoring. Recent studies demonstrated that its absorption signatures within the VNIR spectrum can be resolved using high resolution hyperspectral retrieval algorithms (Borger et al., 2025; Manago et al., 2018; Liu et al., 2022). In addition to atmospheric variables, chlorophyll (CHL) absorption windows were integrated into the analysis. This parameter benefits from an analysis in the hyperspectral VNIR spectrum, since its multiple absorption channels give greater spectral detail and can profoundly enhance the accuracy of the chlorophyll estimations (Giardino et al., 2024; Saberioon et al., 2023). Finally, the spectrum similarity between PRISMA and EnMAP was also compared within the VNIR absorption range of vegetative areas, and to achieve this, the Normalized Difference Vegetation Index (NDVI) was introduced. It accurately quantifies the spectral response of various plant crops, and it also serves as a robust proxy for characterizing and mapping heterogeneous non-vegetated backgrounds, such as urban environments (Leitão et al., 2015; Plajer et al., 2023; Im and Jensen, 2008).

2 Materials and methods

PRISMA and EnMAP missions were both designed to provide globally hyperspectral observations guaranteeing a high-quality level of spectral information and further ensuring global coverage. Data from these missions are distributed under open access licenses

TABLE 1 Main technical, instrumental and operational characteristics of the hyperspectral spaceborne missions PRISMA by ASI, Italy and EnMAP by DLR, Germany.

Satellite properties		PRISMA	EnMAP
Operator		Italian Space Agency, ASI	German Aerospace Center, DLR
Launch date		22 March 2019	1st April 2022
GSD		30 m	30 m
Revisit Time		29 days	27 days
FWHM	VNIR	9–13 nm	8.1 ± 1.0 nm
	SWIR	9–14.5 nm	12.5 ± 1.5 nm
Channels	VNIR	63	91
	SWIR	171	133

within research oriented frameworks and the chance to use them for commercial purposes is also expected under the current policies established by the two space agencies (Italian Space Agency, 2024; The German Aerospace Center, 2025). Each satellite carries an imaging spectrometer, covering the Visible to ShortWave InfraRed (VNIR-SWIR) spectral regions with hundreds of contiguous bands. In the case of PRISMA, it also presents a panchromatic band, with 5 m of GSD, which the EnMAP satellite is not equipped with (Guarini et al., 2018). Table 1 summarizes the main technical characteristics of the missions, highlighting the principal sensor features (Musacchio et al., 2024; Guarini et al., 2018).

As previously introduced, hyperspectral sensors consist of acquisition of a series of images in many adjacent narrow spectral bands, and the precise characterization of spectral configurations is fundamental to understanding the comparative performance of high resolution spaceborne hyperspectral missions. The central wavelength coincidences for the PRISMA and EnMAP missions are not valid for every channel in the VNIR and SWIR spectrum, even though there are several regions of perfect overlap (Chakraborty et al., 2024). Figure 1 shows the distribution of spectral bands for the range of the VNIR spectrum, spreading from 400 to 1,000 nm, where numbers indicate individual band indices, highlighting the variation in band density and sampling intervals between the two systems.

The mismatched number of channels present in the VNIR interval, 63 for PRISMA and 91 for EnMAP, can lead to differences related to the abundance of spectral information that each hyperspectral satellite provides. Furthermore, a discrepancy is highlighted in the extremities involved as observation ranges, considering that PRISMA presents the first band with a central wavelength equal to 402 nm, while EnMAP presents it at 418 nm; and ending channels, before accessing the SWIR hyperspectral cube, are set at 972 nm for PRISMA and 993 nm for EnMAP. As shown, PRISMA distributes 63 bands across the VNIR interval, resulting in a slightly broader spectral sampling in the lower visible ranges. Conversely, EnMAP utilizes a higher density configuration of 91 bands, giving narrower spectral sampling interval that yields finer resolution across identical wavelengths. Despite these differences, no spectral resampling was performed in this study.

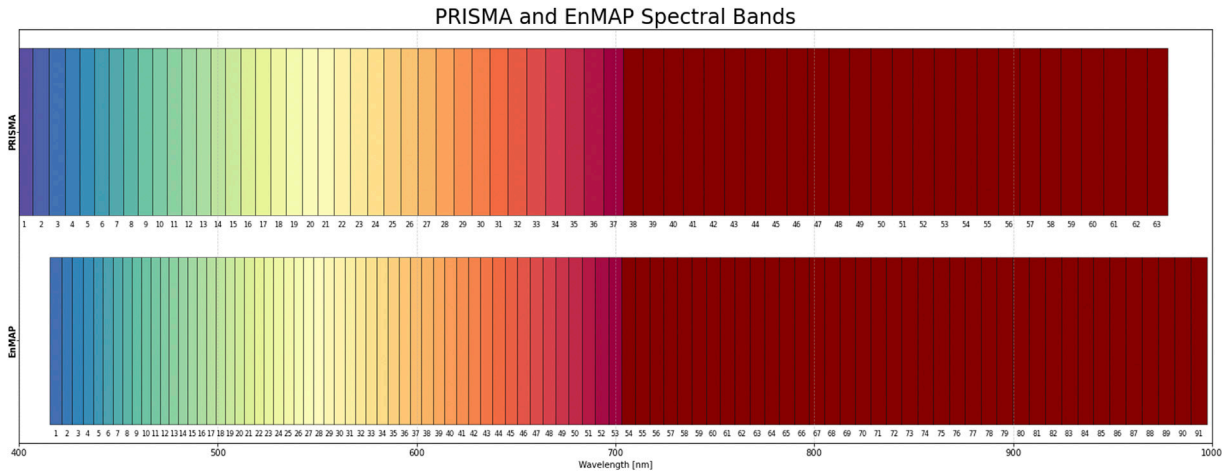


FIGURE 1
Graphical representation of the spectral channels from PRISMA (top) by ASI and EnMAP (bottom) by DLR for the VNIR spectrum range, according to the numerical progression provided by each satellite agency.

TABLE 2 Matching satellite pairs categorized by acquisition time and geographical reference region. Time frame, expressed in hours, indicates the temporal gap between the two acquisitions, and it is calculated by subtracting the passage time of EnMAP, second satellite to acquire in all cases, from the one of PRISMA.

Date	Area	PRISMA acquisition time (UTC)	EnMAP acquisition time (UTC)	Time frame (h)
2024-01-22	Rieti (IT)	10:07:59	10:30:38	00:22:39
2024-04-03	Valencia (SP)	10:49:16	11:35:51	00:46:35
2024-05-05	Opava (CZ)	09:59:35	10:24:06	00:24:31
2024-05-19	Aix-en-Provence (FR)	10:41:16	11:27:23	00:46:07
2024-12-21	Almeria (SP)	11:06:35	11:29:41	00:23:06
2025-05-21	Madrid (SP)	11:43:26	11:09:06	00:34:20
2025-06-24	Toulouse (FR)	11:24:16	10:54:32	00:29:44
2025-07-07	Sevilla (SP)	12:01:43	11:19:53	00:41:50
2025-08-10	Ceuta (SP)	11:44:11	11:07:01	00:37:10
2025-08-10	Toledo (SP)	11:43:04	11:05:55	00:37:09
2025-08-20	Zealand (DK)	10:59:10	10:34:32	00:24:38

Instead, the original bandwidths and center wavelengths of both PRISMA and EnMAP were preserved to maintain the native spectral characteristics of each sensor and avoid introducing artificial smoothing effects. Keeping the spectral channels in their original form allowed for a direct assessment of the actual spectral content of the two data cubes and for establishing robust cross-calibration frameworks between the two platforms.

Spectral similarities between the hyperspectral cubes of the two sensors were assessed relying on two mains statistical approaches. Firstly, the Standard Deviation (STD) Difference was utilized to measure differences in spectral variability and to quantify variations in the absolute magnitude and data dispersion across the spectral bands. In Equation 1 the computation of the STD conducted for each cube is shown (Martinez and Bartholomew, 2017):

$$STD = \sqrt{\frac{\sum_{i=1}^{N}(R_i - \bar{R})^2}{N-1}}, \quad (1)$$

where R_i is the reflectance value of a single band, $\bar{R}$ is the average of reflectances over N samples, which represent the total number of channels.

In addition, the Spectral Angle Mapper (SAM) was introduced, being widely used to measure spectral similarity between two images, as it computes the angle between two spectral vectors typically representing reflectance (or radiance) values for the same target observed by different sensors or under different conditions (Yang et al., 2008). Equation 2 shows the computation of SAM, expressed in radians, after normalization of the shapes of the two vectors:

$$SAM = \arccos\left(\frac{\sum_{i=1}^{N} R_{PRISMA,i} R_{EnMAP,i}}{\sqrt{\sum_{i=1}^{N} R_{PRISMA,i}^2}\sqrt{\sum_{i=1}^{N} R_{EnMAP,i}^2}}\right), \quad (2)$$

where R_{PRISMA} and R_{EnMAP} represent the reflectance values of the two cubes and N is again the total number of spectral bands. A linear interpolation to align the EnMAP data with the PRISMA bands was performed, guaranteeing both arrays match perfectly in size.

2.1 Study areas

The selection of the study areas was driven by strict spatiotemporal matching criteria, limiting data collection to image pairs that exhibit geographical coincidence coverage and temporal concurrence. This approach minimizes differences in acquisition settings in terms of atmospheric, weather and solar zenith angle conditions (Adachi et al., 2019).

In addition, to maintain comparable observation conditions only pairs of scenes showing minimal cloud, haze, dust, smoke, fog or shadow noises were retained for analysis. All selected images are located within the geographical area of the Euro-Mediterranean region, which allows for focusing on both terrestrial and aquatic regions and thus making the comparison of the hyperspectral information valid for a wider variety of background conditions. The involvement of multiple land cover types gives the chance for a more comprehensive evaluation of spectral response characteristics across heterogeneous surfaces. Collection of matching areas begins from January 2023 with the presence of both PRISMA and EnMAP sensors being in orbit, fully operative and properly calibrated, and it ensures a time frame between the two acquisitions inferior to 1 h for the selected cases, as per Table 2. Figure 2 shows locations of each pair of acquisitions across the entire area under analysis.

2.2 Data preprocessing and correction

To avoid additional interference introduced by atmospheric correction algorithms, the analysis was conducted using Level-1 data from both PRISMA and EnMAP. These data contain calibrated radiance measurements at the top of atmosphere, prior to any atmospheric correction or surface reflectance conversion (Giardino et al., 2020; Brell et al., 2024). The use of Level-1 TOA data is motivated by the need to minimize inconsistencies associated with sensor-specific atmospheric correction algorithms, which may introduce systematic differences and affect the robustness of cross-sensor comparisons. By using TOA level spectral data, both hyperspectral datasets are evaluated under more consistent physical

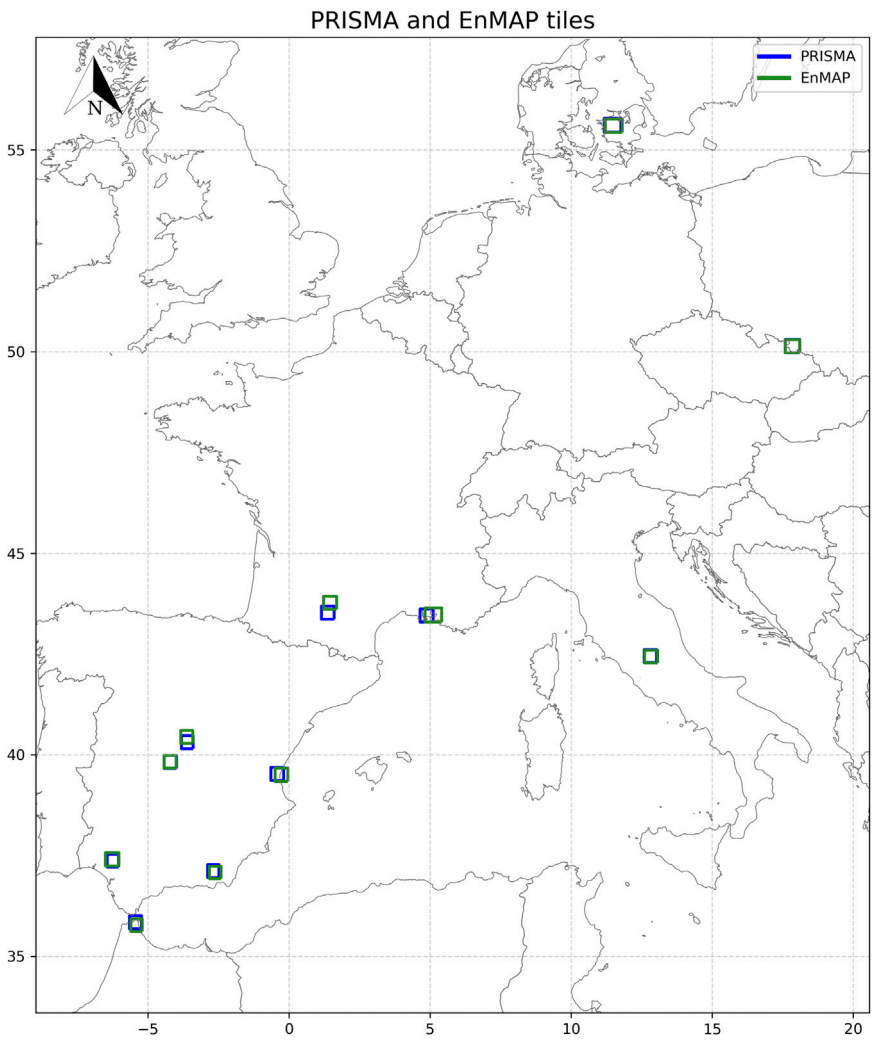


FIGURE 2
Spatial distribution of the acquisition pairs over the Euro-Mediterranean area. Blue tiles indicate PRISMA satellite acquisitions, while green tiles indicate the EnMAP ones.

conditions, reflecting the same surface and atmospheric contributions to the original electromagnetic signal. Several previous studies (Pascual-Venteo et al., 2024; Hadjal et al., 2022; Cremer et al., 2025) have also adopted this approach, avoiding the use of bottom of atmosphere (BOA) reflectance products, to ensure cross-sensor comparability. It should be noted that consistency observed at the TOA level does not necessarily imply equivalent performance in downstream water-quality retrieval applications, such as chlorophyll concentration estimation since the water leaving radiance represents only a small fraction of the total TOA signal and dominant contribution of atmospheric path radiance. However, the objective of this study is limited to assessing the radiometric and spectral consistency between PRISMA and EnMAP at the sensor level. The TOA based framework was intentionally adopted to avoid additional uncertainties introduced by atmospheric correction procedures, particularly in optically complex coastal and inland waters (Hadjal et al., 2022).

To investigate the spectral measurements from different satellite sensors, it was also necessary to account for variations in the atmospheric light paths, which depends on the viewing geometry defined by the relative positions of the sunlight with respect to the sensor (Cooper et al., 2020). In this study, no atmospheric correction was applied, and surfaces were assumed to be ideal Lambertian reflectors, implying isotropic reflection in all directions. Although real surfaces exhibit anisotropic reflectance behavior, this assumption was used as a standardized baseline to create an acceptable comparison framework between the two hyperspectral datasets. In addition, the strict temporal constraint ensures methodological consistency by effectively minimizing the relative variance induced by the Bidirectional Reflectance Distribution Function (BRDF) between the two hyperspectral datasets, since its effects are primarily driven by differences in the sensors' design, orbital paths, and viewing geometry, then time differences (Farhad et al., 2020). By setting the acquisition time gap between the observations to less than 1 hour (Table 2), the variations in solar geometry are constrained and the discrepancies derived by the BRDF effects are mitigated between the PRISMA and EnMAP sensor observations. In this context, to correct the influence of different path lengths caused by variations in viewing geometries, a correction based on the geometric

air mass factor (AMF_G) was applied, as defined in Equation 3 (Palmer et al., 2001):

$$AMF_G = \frac{1}{\cos\theta_s} + \frac{1}{\cos\theta_v} \quad (3)$$

where θ_s stands for the solar zenith angle (SZA) and θ_v for the viewing zenith angle (VZA). These geometric parameters describe the interaction between the incoming solar radiation and the sensor's line of sight at the time of image acquisition and vary for each individual satellite observation (Fraser et al., 1992).

In principle, a more accurate AMF calculation should include the effects of Rayleigh and Mie scattering in the atmosphere and be determined using a radiative transfer model that considers viewing geometry, surface reflectance, vertical distributions of trace gases, as well as cloud and aerosol contributions. However, in this study, only the geometric AMF correction to the radiance data from PRISMA and EnMAP was applied to mitigate inconsistencies of light paths related to viewing geometries. This operation was performed to bring the comparison between the sensors to coincide with the same viewing geometry, also considering solar position.

The computation of reflectance values was then performed to convert radiance measurements into physically meaningful surface properties. This allows a quantitative analysis of spectral characteristics, with reflectance defined as the fraction of incident solar radiation reflected by a surface within a given spectral range (Schaepman-Strub et al., 2006). It describes the interaction between electromagnetic radiation and the surface, and its spectral variability across different wavelengths facilitates the identification and classification of various surface features. To derive reflectance from radiance measurements at TOA level, the Instrumental Spectral Response Function (ISRF), also denoted as the slit function (Beirle et al., 2017), was applied (De Galan and Winefordner, 1968). The use of a Gaussian slit function ensures that the observed spectral variations are primarily attributed to surface properties rather than artifacts arising from sensor spectral response or calibration. The formula (Mobley, 1999) for computing Surface Reflectance (R) at a specific wavelength (λ) is given by Equation 4:

$$R(\lambda) = \frac{\pi * L(\lambda)}{E_s(\lambda) * \cos\theta_s}, \quad (4)$$

where L measures radiances at a given wavelength λ, expressed in $W/m^2/sr/\mu m$, E is the solar spectral irradiance at the TOA in $W/m^2/\mu m$, and θ_s is the SZA in degrees. For the EnMAP dataset, the solar irradiance reference spectrum from Fontenla 2011 solar irradiance model, implemented in MODTRAN 6.0, was convolved (De Los Reyes et al., 2026) to match the instrument's spectral resolution. Conversely, the PRISMA radiance cube was processed using the SOLSPEC reference spectrum (Thuillier et al., 2003). The use of distinct solar irradiance spectra reflects the respective processing chains adopted by the two space agencies, which internally convert TOA radiances into reflectance using mission-specific reference datasets. The application of the two official Irradiance Reference Spectra, defined by the operational teams of the satellites, was performed also to assess the interoperability of the reflectance product (Level-2), as distributed by the respective agencies. The spectral behaviors of the two high resolution irradiance spectra are shown in Figure 3, along with their relative differences expressed as a function of the wavelength. The spectral range considered in this study is the VNIR channel spanning from 400 to 1,000 nm.

For this analysis, the PRISMA hyperspectral cube underwent the AMF_G correction, while the EnMAP cube was retained in its original

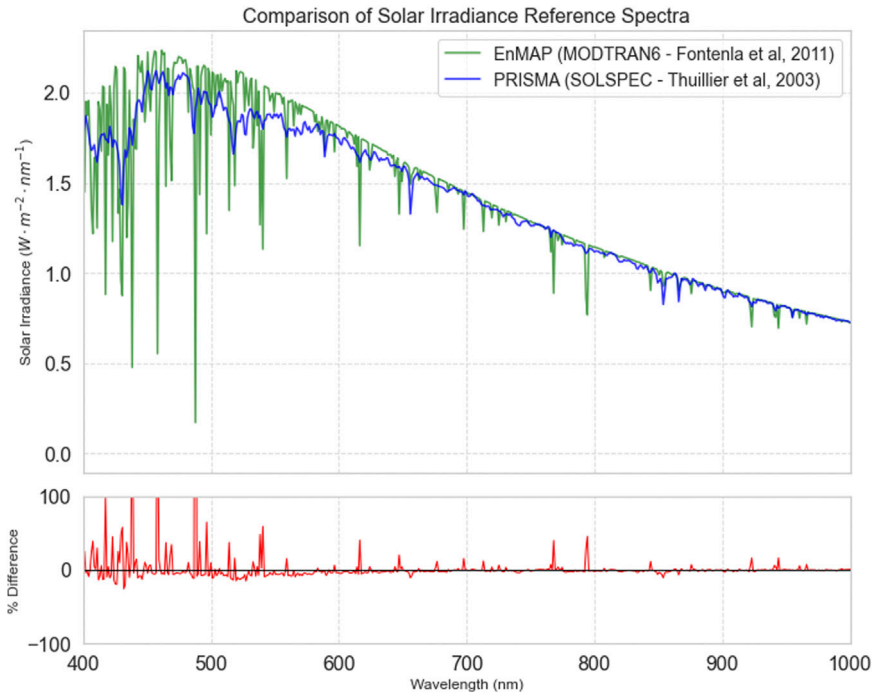


FIGURE 3
Comparison of the Solar Irradiance Reference Spectra considered for PRISMA mission (SOLSPEC, in blue) and EnMAP one (MODTRAN6, in green). At the bottom of the image, in red, the percentage difference between the two spectra is shown.

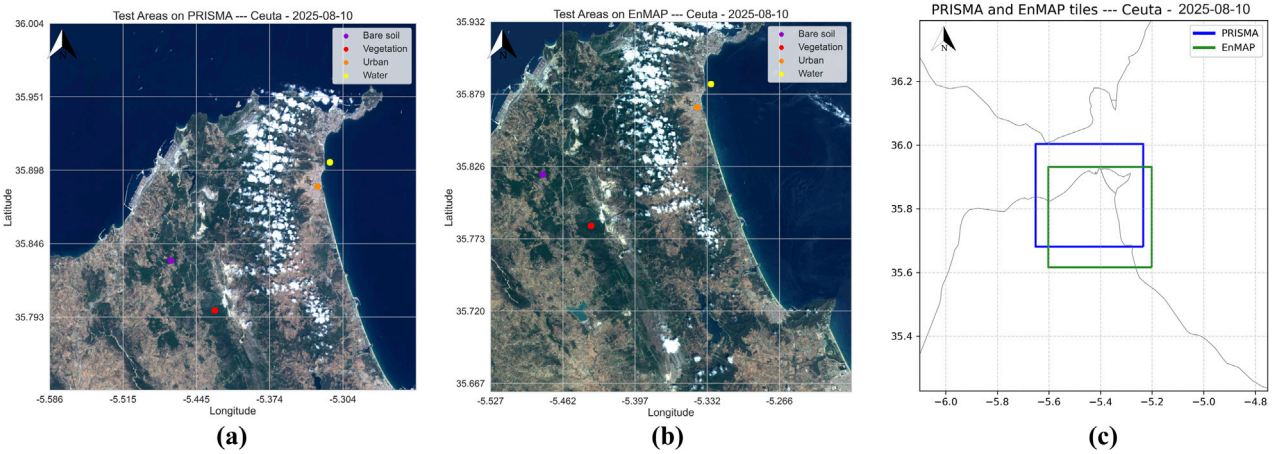


FIGURE 4
Locations of the areas analyzed for each land cover class in the PRISMA **(a)** and EnMAP **(b)** scenes, along with the positioning of acquisition tiles **(c)** over Ceuta (SP) on 10 of August 2025.

form. For each PRISMA acquisition, a mean value was computed by integrating the geometrical angle parameters derived from the corresponding Level-2C data products provided by ASI (ASI-Italian Space Agency, 2021). This geocoded processing level includes additional metadata elements, such as SZA and VZA, together with other relevant geometrical orientation attributes. To ensure a robust cross-sensor comparison, geometric adjustment applied to the PRISMA hyperspectral data was released using Equation 5:

$$R'_{PRISMA} = \frac{R_{PRISMA}}{AMF_{G,PRISMA}} * AMF_{G,EnMAP} \quad (5)$$

where R_{PRISMA} is the initial TOA reflectance and R'_{PRISMA} is the final geometric adjusted PRISMA reflectance, used for comparison with EnMAP TOA reflectance. The corrected PRISMA cube thereby supports a more accurate and unbiased inter-mission comparison process, minimizing discrepancies that may appear from different sensor specific characteristics.

2.3 Spectral signatures comparison

The spectral analysis was designed on four main land cover classes: bare soil, urban areas, vegetation and water bodies. These categories were selected for their distinct and recurrent spectral signatures, as well as their relevance to environmental applications, to ensure comprehensive representation of both natural and anthropogenic surface types (Anderson, 1976). The inclusion of these specific land covers allows for an extensive characterization of spectral behaviors across diverse environments; however, not all image pairs include all four land cover classes. Complete coverage of the four land cover types was available for the scenes acquired over Rieti (IT), Valencia (SP), Aix-en-Provence (FR), Madrid (SP), Toulouse (FR), Ceuta (SP), Toledo (SP), Zealand (DK).

For each identified class, a subset of 25 contiguous representative pixels was selected from the central area of homogeneous regions to minimize spectral contamination from neighboring surfaces. This sampling approach attempts to reduce the effects of mixed or edge-pixels within transitional zones, thereby improving spectral uniformity across classes. A representative example is presented in Figure 4, where the selected regions for each land cover class are shown in different colors for the acquisition over the city of Ceuta (SP) on 10 August 2025, along with the corresponding alignment of PRISMA and EnMAP image tiles. Figures 5, 6 provide zoomed-

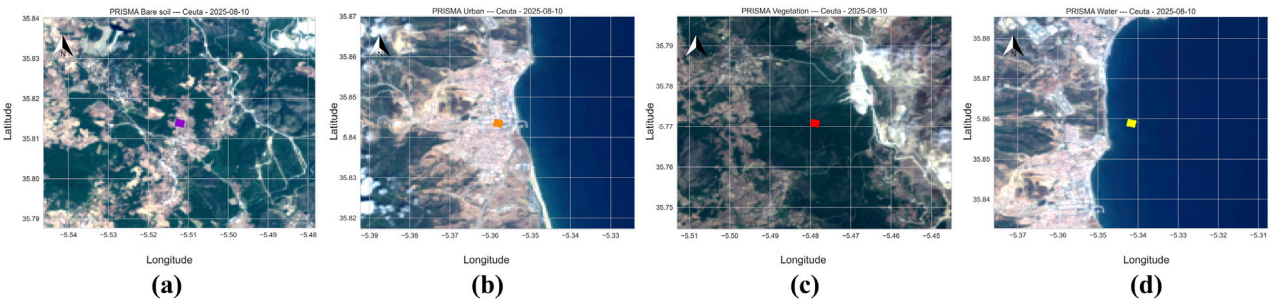


FIGURE 5
Detailed view of the PRISMA acquisition over the selected areas for bare soil **(a)**, urban areas **(b)**, vegetation **(c)** and water **(d)**.

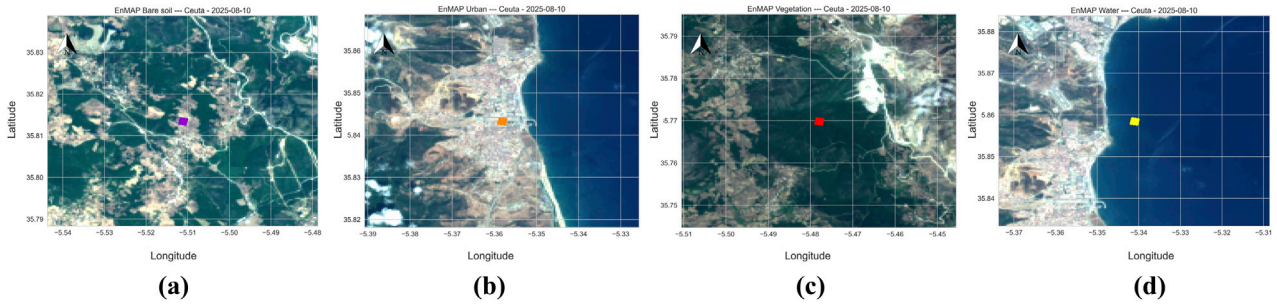


FIGURE 6
Detailed view of the EnMAP acquisition over the selected areas for bare soil **(a)**, urban areas **(b)**, vegetation **(c)** and water **(d)**.

TABLE 3 **VNIR spectral ranges observed for the analysis of chlorophyll (CHL), nitrogen dioxide (NO_2) and normalized difference vegetation index (NDVI), according to relevant literature.**

Parameter	Spectrum range (nm)	References
CHL	400–480, 600–700	Zscheile and Comar (1941)
NO_2	420–500	Xue et al. (2000)
NDVI	750–940	Fava et al. (2009)

in views of the selected study areas for each surface classification, respectively for PRISMA and EnMAP.

Spectral comparisons were first conducted across the full VNIR spectrum range and subsequently within specific spectral intervals relevant to targeted environmental monitoring parameters. Specific focus was given to spectral regions associated with key atmospheric and biophysical parameters and indices, including chlorophyll (CHL), nitrogen dioxide (NO_2) and normalized difference vegetation index (NDVI). The ability to examine such narrow spectral domains is inherently enabled by hyperspectral image observations, which provide information at fine wavelength increments. In this study, the spectral ranges shown in Table 3 within the VNIR channels were analyzed for the environmental parameters mentioned.

3 Results

The results of the spectral comparison were presented as spectral signatures to highlight the preliminary similarities and differences in the reflectance between PRISMA and EnMAP. For each land cover class, the same comparisons were performed to illustrate the characteristics of spectral signatures captured by the two hyperspectral sensors. Examples of the spectral behaviors for the vegetation land cover type are shown in Figures 7–9 for selected sample cases.

The reported spectral signatures consistently display the well-known reflectance pattern of vegetated surfaces, including the pronounced increase in reflectance across the near-infrared region, typically between 700 and 900 nm (Hoffer and Chris, 1969). However, this feature is less evident in several scene cases, particularly those obtained over Rieti (IT) on 22 January 2024, Valencia (SP) on 3 April 2024, and Almeria (SP) on 21 December

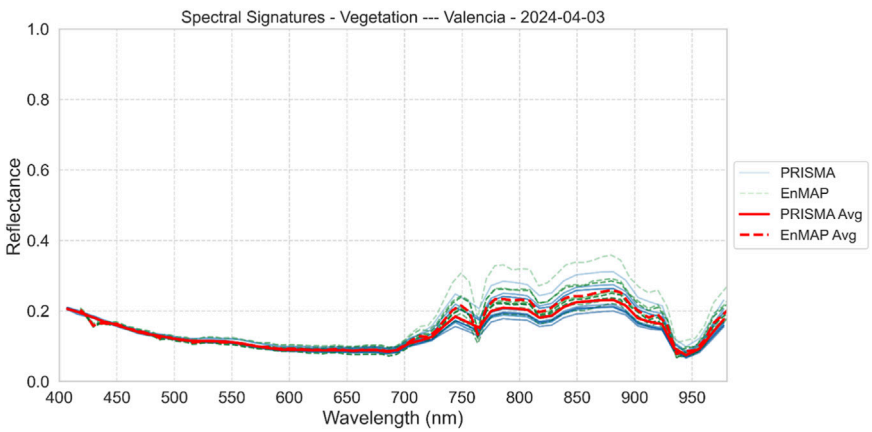


FIGURE 7
Spectral signature from PRISMA (solid lines with blue shades) and EnMAP (dashed line with green shades) over a vegetated area for the Valencia (SP) scene acquired on 2024-04-03. In red the spectral signature obtained averaging reflectance values for all selected pixels.

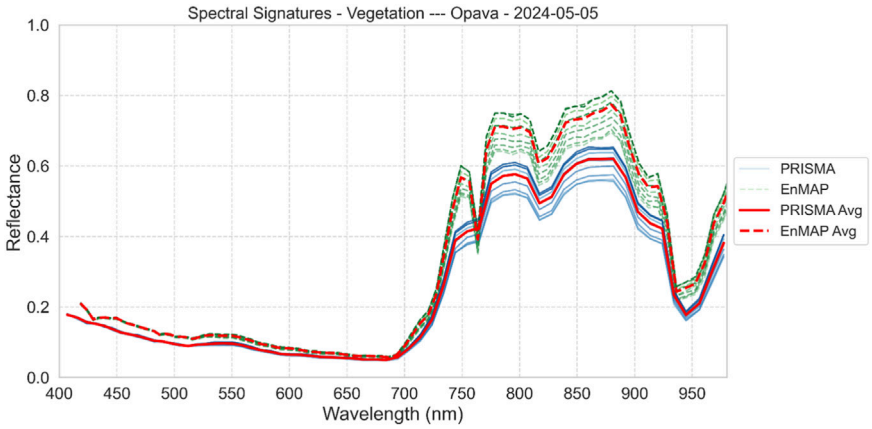


FIGURE 8
Spectral signature from PRISMA (solid lines with blue shades) and EnMAP (dashed line with green shades) over a vegetated area for the Opava (CZ) scene acquired on 2024-05-05. In red the spectral signature obtained averaging reflectance values for all selected pixels.

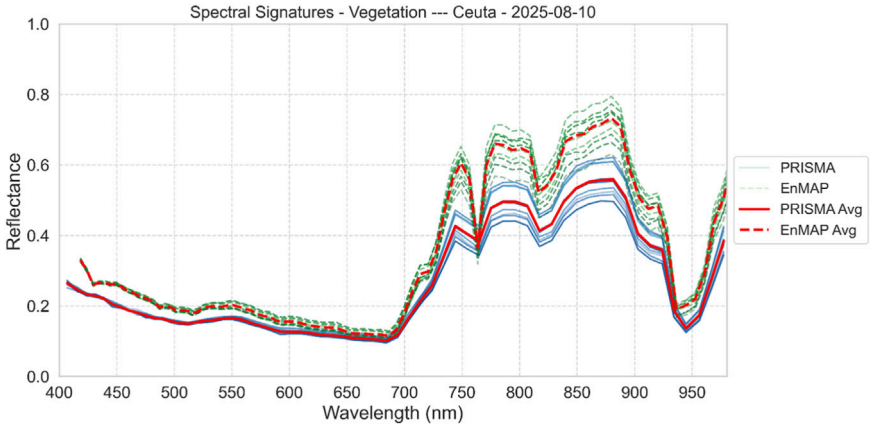


FIGURE 9
Spectral signature from PRISMA (solid lines with blue shades) and EnMAP (dashed line with green shades) over a vegetated area for the Ceuta (SP) scene acquired on 2025-08-10. In red the spectral signature obtained averaging reflectance values for all selected pixels.

2024. These three images correspond to the observations acquired during colder seasons, where reduced vegetation vigor and lower surface temperatures likely contributed to a weaker NIR reflectance response compared to other periods (Akakpo et al., 2025).

The consistency across the different land cover classes between the two sensors was further assessed to evaluate overall spectral coherence by examining mean reflectance values obtained by averaging the 25 sampled contiguous pixels belonging to each land class. The evaluation was conducted using a scatter plot displaying the relationship between the average reflectance derived from the PRISMA and EnMAP data, as revealed in Figure 10.

For most scenes, a good coherence is identified between the two hyperspectral measurements with a high correlation, showing a total R^2 equal to 0.981 and indicating then a comparable spectral behavior. However, the scenes acquired over Madrid (SP) on 21May 2025 and Sevilla (SP) on 7 July 2025 show a greater deviation. In both cases, the EnMAP reflectance values exhibit a systematic increase relative to PRISMA across all evaluated land cover classes, with a more evident incidence for the bare soil class. The repetition of this distanced behavior across all selected land cover classes further supports the assumption that the spectral responses recorded by the two satellites in both these scene pairs, Madrid (SP) and Sevilla (SP), are slightly uncorrelated. This is additionally highlighted by the computed RMSE between the two datasets, which exhibit noticeably larger differences, as reported just for the bare soil background equal to 0.238 in Madrid (SP) and 0.263 in Sevilla (SP).

An additional analysis was conducted on selected wavelength intervals within the VNIR spectrum in order to identify spectral similarities between PRISMA and EnMAP for environmental applications. Understanding the behavior of key environmental parameters within these targeted spectral ranges is meaningful for assessing the compatibility and interoperability of the two hyperspectral sensors.

Examination of narrow spectral intervals increases sensitivity to discrepancies between different datasets and

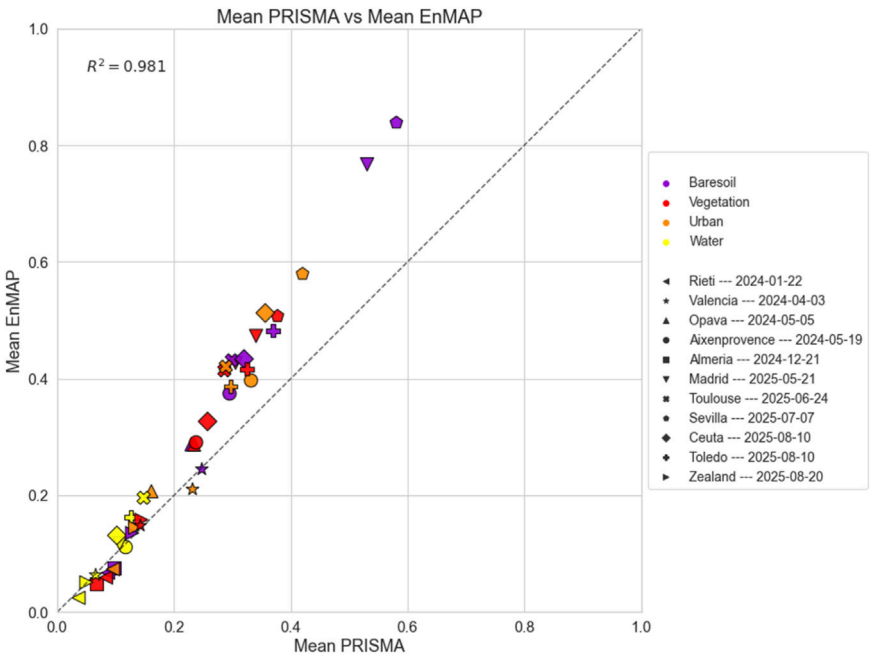


FIGURE 10
Scatter plot comparing the average reflectance values between PRISMA and EnMAP acquisitions according to the background (violet is used for bare soil, orange for urban, red for vegetation and yellow for water) and the observation area, indicated with different markers as per the legend. Each marker shows results for all land cover classes present in the satellite acquisition, land cover classes not captured are omitted, e.g., water surface class is not present for several of the selected scenes.

sensor platforms. However, it should be recalled that PRISMA and EnMAP differ in their spectral resolution and band configuration, which directly affects comparability within restricted spectral windows. The number of spectral channels was eventually left unchanged, avoiding further modifications to the reflectance cubes, in order to better outline the actual spectral significance of each subrange of hyperspectral bands. The comparison was then carried out for the wavelength ranges sensitive to CHL, NO_2, and vegetation through the NDVI determined according to the absorption characteristics of the respective targets and the specifications of the two instruments within the VNIR spectral window, as reported in Table 3. Figures 11–13 present the comparison of reflectance features for the four corresponding spectral windows over the vegetated land cover class derived from the two hyperspectral sensors.

Overall, the reflectance from the selected collocated samples shows only minor variability between PRISMA and EnMAP. The exception is the NDVI sensitive wavelength ranges (750–940 nm), where both sensors show relatively large reflectance variability, both within their individual pixel distributions and between the two instruments, across most land cover types. Figure 14 summarizes the differences in the standard deviations of reflectance for the four spectral ranges depending on surface types for all the pixels selected in the analysis.

A clear trend of increasing STD difference is observed moving towards the near IR ranges of the spectrum. The NDVI sensitive spectral range, covering 750–940 nm window, shows higher variance and median differences compared to the VIS range, introducing STD differences up to 0.334. This appears consistent across most land cover types, including bare soil, urban, and vegetation. The exception stands in the water surfaces responses which present the weakest variation in terms of standard deviation differences, due to the strong liquid water absorption in the NIR region, presenting then reflectances close to the minimum (Curcio and Petty 1951). Truly, water class exhibits the highest stability across all parameters because of its low and uniform reflectance profile, confirmed also in the water reflectance patterns identified in the spectral signature representations. Across all four spectral subranges, the water background consistently yields the lowest median STD differences, and this indicates a high level of agreement between the PRISMA and EnMAP sensors when observing aquatic environments.

4 Discussion

Quantitative evaluation of the extracted spectral signatures was performed using statistical indicators designed to assess spectral similarity and variability. In particular, the SAM was employed to quantify the degree of correspondence between the PRISMA and EnMAP datasets. Since SAM requires equal length spectral vectors, the normalization was performed using linear interpolation to project EnMAP spectrum onto the wavelength grid of PRISMA to ensure wavelength alignment and consistent spectral dimensionality. Table 4 reports the SAM results, expressed in radians, for each pair of acquisitions following the normalization of the sizes of the two hyperspectral cubes to enable a consistent comparison.

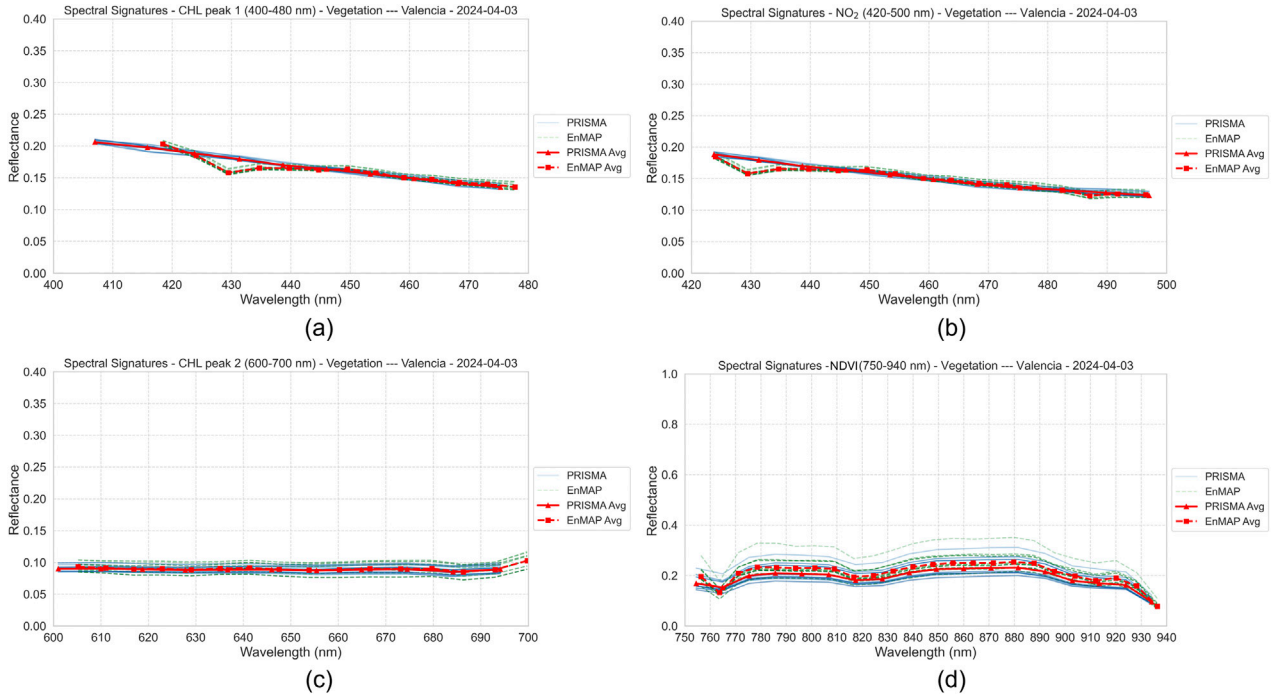


FIGURE 11
Spectral signature from PRISMA (solid lines with blue shades) and EnMAP (dashed line with green shades) in sensitivity ranges for CHL **(a,c)**, NO_2 **(b)** and NDVI **(d)** over a vegetated area for the Valencia (SP) scene acquired on 2024-04-03. In red the spectral signature obtained averaging reflectance values for all selected pixels.

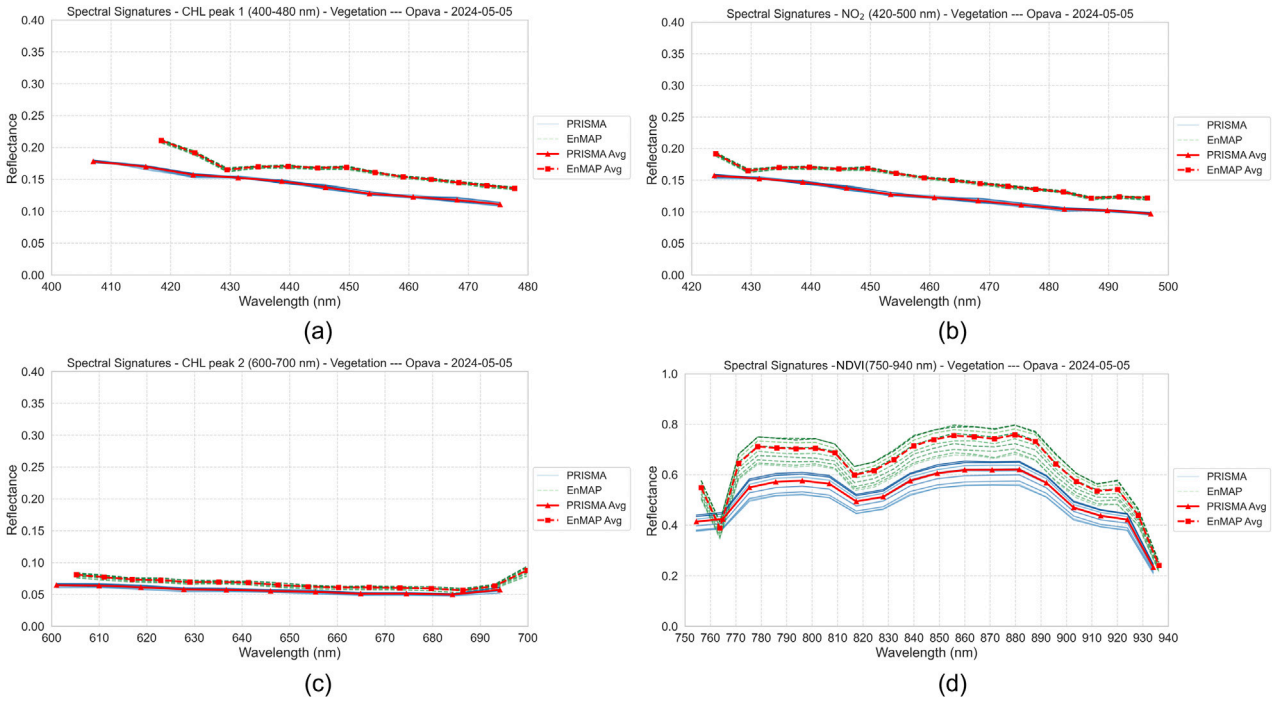


FIGURE 12
Spectral signature from PRISMA (solid lines with blue shades) and EnMAP (dashed line with green shades) in sensitivity ranges for CHL **(a,c)**, NO_2 **(b)** and NDVI **(d)** over a vegetated area for the Opava (CZ) scene acquired on 2024-05-05. In red the spectral signature obtained averaging reflectance values for all selected pixels.

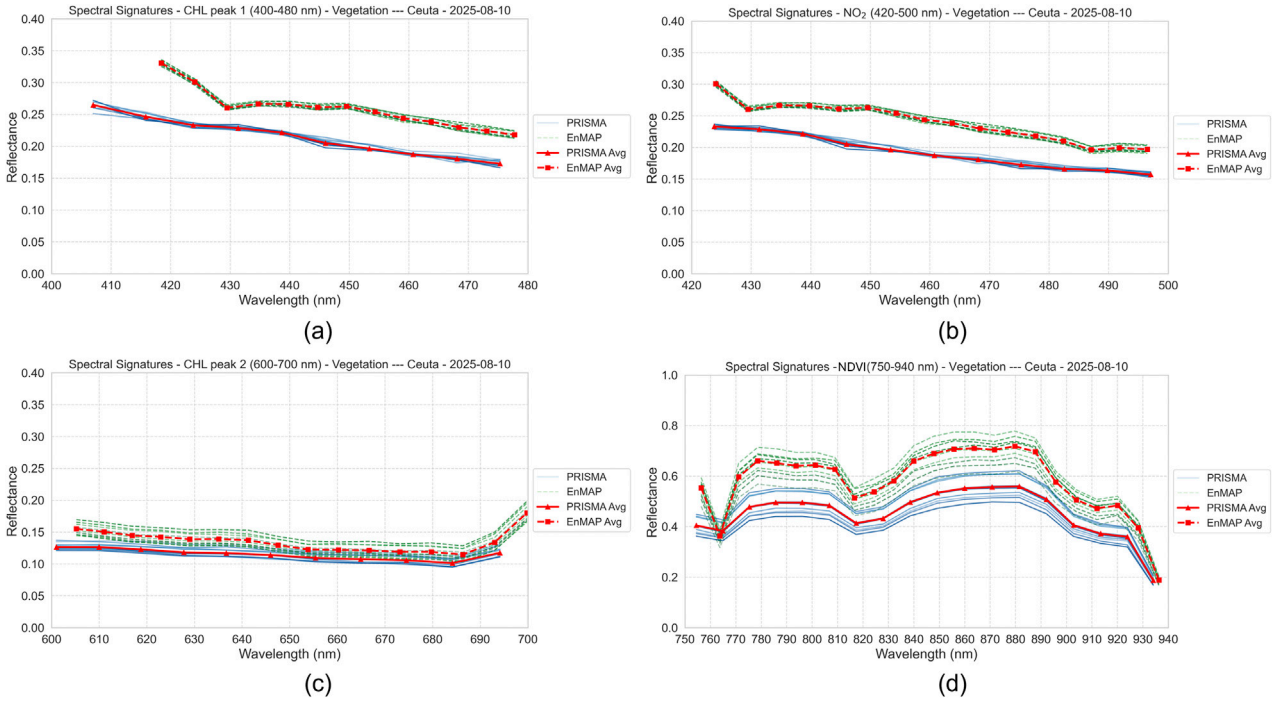


FIGURE 13
Spectral signature from PRISMA (solid lines with blue shades) and EnMAP (dashed line with green shades) in sensitivity ranges for CHL **(a,c)**, NO_2 **(b)** and NDVI **(d)** over a vegetated area for the Ceuta (SP) scene acquired on 2025-08-10. In red the spectral signature obtained averaging reflectance values for all selected pixels.

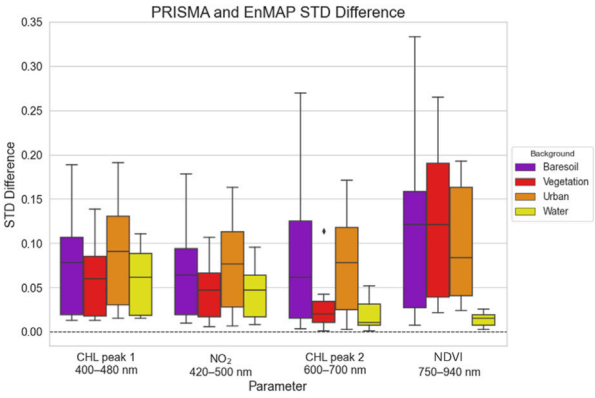


FIGURE 14
Comparison of the Standard Deviation (STD) difference between PRISMA and EnMAP hyperspectral data across the four distinct spectral parameter windows (CHL peak 1, NO_2, CHL peak 2 and NDVI). The variations are grouped by surface background type: bare soil (purple), vegetation (red), urban (orange) and water (yellow). The dashed horizontal line at 0 represents the statistical agreement between the two sensors.

TABLE 4 The SAM values calculated between PRISMA and EnMAP reflectance for each test area over the full VNIR spectrum.

Date	Area	SAM (rad) ↓
2024-01-22	Rieti (IT)	0.0719
2024-04-03	Valencia (SP)	0.0774
2024-05-05	Opava (CZ)	0.0499
2024-05-19	Aix-en-Provence (FR)	0.0722
2024-12-21	Almeria (SP)	0.0662
2025-05-21	Madrid (SP)	0.0558
2025-06-24	Toulouse (FR)	0.0517
2025-07-07	Sevilla (SP)	0.0539
2025-08-10	Ceuta (SP)	0.0626
2025-08-10	Toledo (SP)	0.0463
2025-08-20	Zealand (DK)	0.0624

As lower SAM values indicate smaller angles between the compared spectra and thus stronger spectral agreement, these results provide meaningful insight into the relative consistency of the two sensors. The SAM values obtained are consistently low across all observations. This indicates a generally high level of spectral similarity across the two reflectance cubes, remaining these results below the 0.1 rad threshold, often used as a benchmark for guaranteeing accurate spectral similarity (Lamelas-Gracia et al., 2019). In addition, no distinct correlations are identified by analyzing seasonal or geographical trends, as the slightest SAMs, around 0.04 rad, belong to areas of different latitudes and acquired at different times of the year.

The SAM analysis was also performed according to the spectral windows identified in Table 3 for selected environmental parameter.

TABLE 5 Results of SAM calculated between PRISMA and EnMAP reflectance values divided by test area over the NDVI and NO_2 spectral windows.

Date	Area	SAM (rad) ↓	
		NDVI (750–940 nm)	NO_2 (420–500 nm)
2024-01-22	Rieti (IT)	0.0969	0.0385
2024-04-03	Valencia (SP)	0.0817	0.0382
2024-05-05	Opava (CZ)	0.0444	0.0451
2024-05-19	Aix-en-Provence (FR)	0.0681	0.0360
2024-12-21	Almeria (SP)	0.0464	0.0478
2025-05-21	Madrid (SP)	0.0665	0.0410
2025-06-24	Toulouse (FR)	0.0536	0.0464
2025-07-07	Sevilla (SP)	0.0456	0.0354
2025-08-10	Ceuta (SP)	0.0547	0.0414
2025-08-10	Toledo (SP)	0.0544	0.0470
2025-08-20	Zealand (DK)	0.0615	0.0463

In this case, to ensure consistency across the two datasets, an interpolation was applied to standardize the dimensions of the data shapes, adjusting them to be uniform and comparable. Table 5 summarizes the SAM values for the NDVI and NO_2 sensitive wavelength ranges as a representative sample.

For most sampling sites, the NDVI spectral window consistently exhibits higher SAM values than the NO_2 one, indicating again relatively lower spectral similarity between PRISMA and EnMAP moving towards the IR regions of the spectrum. The relatively higher SAM values within the 750–940 nm range can be attributed to the presence of water vapor absorption features (Curcio and Petty 1951), which may increase the angular divergence between the sensor measurements in the NIR region. Overall, even for the vegetative sensitiveness window represented by the NDVI, the SAM analysis demonstrates a strong spectral match between the two sensors, still demonstrating not to exceed 0.1 rad, as a reference value for good spectral similarity (Lamelas-Gracia et al., 2019).

The closer look at wavelengths sensitive to vegetative environments within the VNIR domain (750–940 nm) shows largest discrepancies also in terms of standard deviation. In this region, STD differences reach around 0.067, while lower STD values around 0.045 are obtained in the NO_2 sensitive range (420–500 nm). Similarly, spectral regions associated with chlorophyll absorption features (400–480 nm and 600–700 nm) exhibit relatively low STD values (~0.051), indicating strong agreement irrespective of the underlying surface type. These variations suggest that while the spectral agreement achieves robust accuracy across high absorption features, atmospheric interferences within the vegetation sensitive domain introduce a higher degree of uncertainty that may require closer inspection.

5 Conclusion

This study presents a comprehensive evaluation of the spectral consistency and potential discrepancies between the hyperspectral missions PRISMA and EnMAP. The strength of the investigation lies in the extensive set of co-located acquisitions, including diverse land cover types and background conditions, which enhances the robustness and representativeness of the spectral analysis results. The consistency of the acquisition conditions inherent to the two sensor platforms takes into account the differences in geometrical viewing angles. This is also compensated with the selection of processing level products with no atmospheric correction applied, to ensure that the comparison is focused on the instrumental spectral response characteristics.

The spectral comparison highlights a satisfactory level of agreement between hyperspectral datasets acquired under analogous background conditions. Nevertheless, the analysis results reveal slight, but statistically significant, variations in spectral correspondence, while still indicating a generally strong level of interchangeability between PRISMA and EnMAP sensors across the VNIR spectral range. This consistency is observed across all investigated land cover types, for which the spectral response profiles remain highly congruent within each image pair. A more detailed examination indicates that the VNIR spectrum around 750–940 nm wavelength ranges presents the largest discrepancies, as reflected by increased standard deviation values relative to other spectral intervals (up to 0.067). In any case, all analyzed pairs demonstrated high spectral similarities with SAM values below 0.1 rad, confirming, but when focusing on specific VNIR subranges associated with key atmospheric constituents, the NDVI sensitive region consistently shows higher SAM values (lower similarities) across all sampling sites compared to other spectral windows, such as those sensitive to NO_2. The relatively reduced spectral consistency in NDVI relevant wavelengths could be attributed to the more pronounced interference from water vapor absorption features in the red and near-infrared regions compared to the visible spectrum.

The current approach remains susceptible to variability induced by atmospheric contributions such as the scattering and absorption effects. Further improvements could be achieved

by employing a common and standardized atmospheric correction algorithm to both hyperspectral data cubes. A unified correction framework would minimize such influences, thereby significantly improving the interpretability and cross-scene comparability of the results. In addition, the current analysis has mainly focused on the VNIR channels, while future work can extend the established spectral analysis to the Short-Wave Infrared (SWIR) region, typically 1,000–2,500 nm. The SWIR spectrum is particularly valuable for atmospheric applications, as it includes key absorption features of trace gases such as carbon dioxide (CO_2) and methane (CH_4), enabling for their detection and quantification using hyperspectral information.

Finally, the integration of multi-temporal datasets represents a valuable direction for future research. Such an approach would enable systematic assessment of spectral variability driven by factors including viewing geometries, seasonal vegetation dynamics, and surface moisture contents. This extended analysis will provide a more robust understanding of the temporal stability of the spectral responses and support a more generalizable characterization of the consistency between PRISMA and EnMAP. At the same time, due to similarities in sensor characteristics between PRISMA and EnMAP with the upcoming CHIME mission, the outcomes of the present study may be relevant in the perspective of multiple interoperability of next gen of hyperspectral open access data.

Data availability statement

The raw data supporting the conclusions of this article will be made available by the authors, without undue reservation.

Author contributions

VL: Conceptualization, Writing – original draft. SS: Conceptualization, Methodology, Supervision, Writing – review and editing. DD: Conceptualization, Methodology, Supervision, Writing – review and editing. FD: Methodology, Supervision, Writing – review and editing. DL: Methodology, Supervision, Writing – review and editing.

Funding

The author(s) declared that financial support was not received for this work and/or its publication.

Acknowledgements

The authors would like to express their gratitude to the Italian Space Agency (ASI) and the German Aerospace Center (DLR) for providing the PRISMA and EnMAP datasets under their respective scientific user agreements.

Conflict of interest

Authors VL and DD were partners of Blue Dot Observation Srl.

The remaining author(s) declared that this work was conducted in the absence of any commercial or financial relationships that could be construed as a potential conflict of interest.

Generative AI statement

The author(s) declared that generative AI was not used in the creation of this manuscript.

Any alternative text (alt text) provided alongside figures in this article has been generated by Frontiers with the support of artificial intelligence and reasonable efforts have been made to ensure accuracy, including review by the authors wherever possible. If you identify any issues, please contact us.

Publisher's note

All claims expressed in this article are solely those of the authors and do not necessarily represent those of their affiliated organizations, or those of the publisher, the editors and the reviewers. Any product that may be evaluated in this article, or claim that may be made by its manufacturer, is not guaranteed or endorsed by the publisher.

References

Adachi, Y., Kikuchi, R., Obata, K., and Yoshioka, H. (2019). Relative azimuthal-angle matching (RAM): a screening method for GEO-LEO reflectance comparison in middle latitude forests. *Remote Sens.* 11 (9), 1095. doi: 10.3390/rs11091095

Akakpo, B. A., Padonou, E. A., Ouedraogo, V., Ahouandjinou, E. B., Okhimamhe, A. A., Ibrahim, H., et al. (2025). Exploring urban vegetation index trends, seasonal variations, and their correlation with temperature in Benin (west Africa). *Urban Resil. Sustain.* 3 (2), 154–171. doi: 10.3934/urs.2025007

Anderson, J. R. (1976). *A Land Use Land Cover Classification System Use Remote Sensor Data* 964. US Government Printing Office. doi: 10.3133/pp964

ASI-Italian Space Agency (2021). PRISMA algorithm theoretical basis document (ATBD), issue 1, date 14/12/2021. Available online at: https://prisma.asi.it/missionselect/docs/PRISMA%20ATBD_v1.pdf (accessed on April 14, 2025).

Baumgartner, A., Gege, P., Köhler, C., Lenhard, K., and Schwarzmaier, T. (2012). Characterisation methods for the hyperspectral sensor HySpex at DLR's calibration home base. *Sensors, Syst. Next-Generation Satell. XVI* 8533, 371–378. doi: 10.1117/12.974664

Beirle, S., Lampel, J., Lerot, C., Sihler, H., and Wagner, T. (2017). Parameterizing the instrumental spectral response function and its changes by a super-gaussian and its derivatives. *Atmos. Meas. Tech.* 10 (2), 581–598. doi: 10.5194/amt-10-581-2017

Borger, C., Beirle, S., Butz, A., Scheidweiler, L. O., and Wagner, T. (2025). High-resolution observations of NO2 and CO2 emission plumes from EnMAP satellite measurements. *Environ. Res. Lett.* 20 (4), 044034. doi: 10.1088/1748-9326/adc0b1

Brell, M., Guanter, L., Segl, K., Chabrillat, S., Scheffler, D., Soppa, M., et al. (2024). *Assessment of Enmap Data Quality Through Global Product Validation Activities.*

Calin, M. A., Calin, A. C., and Nicolae, D. N. (2021). Application of airborne and spaceborne hyperspectral imaging techniques for atmospheric research: past, present, and future. *Appl. Spectrosc. Rev.* 56 (4), 289–323. doi: 10.1080/05704928.2020.1774381

Candela, L., Formaro, R., Guarini, R., Loizzo, R., Longo, F., and Varacalli, G. (2016). "The PRISMA mission," in *2016 IEEE International Geoscience and Remote Sensing Symposium (IGARSS)* (IEEE), 253–256.

Canero, F. M., Rodriguez-Galiano, V., and Cardenas-Martinez, A. (2024). "Comparing hyperspectral spaceborne EnMAP, PRISMA and DESIS missions for soil salinity mapping in a high-saline and semi-arid area," in *IGARSS 2024-2024 IEEE International Geoscience and Remote Sensing Symposium* (IEEE), 6735–6739.

Caporusso, G., Lopinto, E., Lorusso, R., Loizzo, R., Guarini, R., Daraio, M. G., et al. (2020). "The hyperspectral prisma mission in operations," in *IGARSS 2020-2020 IEEE International Geoscience and Remote Sensing Symposium* (IEEE), 3282–3285.

Carmona, E., Chabrillat, S., Fischer, S., Habermeyer, M., La Porta, L., Mühle, H., et al. (2024). "ENMAP operations status," in *IGARSS 2024-2024 IEEE International Geoscience and Remote Sensing Symposium* (IEEE), 292–295.

Chakraborty, R., Rachdi, I., Thiele, S., Booysen, R., Kirsch, M., Lorenz, S., et al. (2024). A spectral and spatial comparison of satellite-based hyperspectral data for geological mapping. *Remote Sens.* 16 (12), 2089. doi: 10.3390/rs16122089

Cheng, M. F., Mukundan, A., Karmakar, R., Valappil, M. A. E., Jouhar, J., and Wang, H. C. (2025). Modern trends and recent applications of hyperspectral imaging: a review. *Technologies* 13 (5), 170. doi: 10.3390/technologies13050170

Cooper, M. J., Martin, R. V., Henze, D. K., and Jones, D. (2020). Effects of *a priori* profile shape assumptions on comparisons between satellite NO 2 columns and model simulations. *Atmos. Chem. Phys.* 20 (12), 7231–7241. doi: 10.5194/acp-20-7231-2020

Cremer, N., Alonso, K., Doxani, G., Chlus, A., Thompson, D. R., Brodrick, P., et al. (2025). Atmospheric correction inter-comparison eXercise, ACIX-III land: an assessment of atmospheric correction processors for EnMAP and PRISMA over land. *Remote Sens.* 17 (23), 3790. doi: 10.3390/rs17233790

Curcio, J. A., and Petty, C. C. (1951). The near infrared absorption spectrum of liquid water. *J. Optical Society Am.* 41 (5), 302–304. doi: 10.1364/josa.41.000302

De Galan, L., and Winefordner, J. D. (1968). Slit function effects in atomic spectroscopy. *Spectrochim. Acta Part B At. Spectrosc.* 23 (4), 277–289. doi: 10.1016/0584-8547(68)80007-2

De los Reyes, R., Langheinrich, M., Eckert, T. M., and Bachmann, M. (2026). EnMAP ground segment: level 2A processor (atmospheric correction over land) ATBD (issue 2.5; doc. ID EN-PCV-TN-6007). *Dtsch. Zent. für Luft- Raumfahrt e.V. (DLR)*. Available online at: https://www.enmap.org/data/doc/EN-PCV-TN-6007_Level_2A_Processor_Atmospheric_Correction_Land.pdf (Accessed April 8, 2026).

Farhad, M. M., Kaewmanee, M., Leigh, L., and Helder, D. (2020). Radiometric cross calibration and validation using 4 angle BRDF model between landsat 8 and sentinel 2A. *Remote Sens.* 12 (5), 806. doi: 10.3390/rs12050806

Fava, F., Colombo, R., Bocchi, S., Meroni, M., Sitzia, M., Fois, N., et al. (2009). Identification of hyperspectral vegetation indices for mediterranean pasture characterization. *Int. J. Appl. Earth Observation Geoinformation* 11 (4), 233–243. doi: 10.1016/j.jag.2009.02.003

Fraser, R. S., Ferrare, R. A., Kaufman, Y. J., Markham, B. L., and Mattoo, S. (1992). Algorithm for atmospheric corrections of aircraft and satellite imagery. *Int. J. Remote Sens.* 13 (3), 541–557. doi: 10.1080/01431169208904056

Giardino, C., Bresciani, M., Braga, F., Fabbretto, A., Ghirardi, N., Pepe, M., et al. (2020). First evaluation of PRISMA level 1 data for water applications. *Sensors* 20 (16), 4553. doi: 10.3390/s20164553

Giardino, C., Bresciani, M., Fabbretto, A., Pellegrino, A., Panizza, L., Matta, E., et al. (2024). "Prisma products and applications for aquatic ecosystems," in *IGARSS 2024-2024 IEEE International Geoscience and Remote Sensing Symposium* (IEEE), 2251–2254.

Green, R. O. (2022). "The NASA Earth venture instrument, Earth surface mineral dust source investigation (EMIT)," in *IGARSS 2022-2022 IEEE International Geoscience and Remote Sensing Symposium* (IEEE), 5004–5006.

Green, R. O., Eastwood, M. L., Sarture, C. M., Chrien, T. G., Aronsson, M., Chippendale, B. J., et al. (1998). Imaging spectroscopy and the airborne visible/infrared imaging spectrometer (AVIRIS). *Remote Sensing Environment* 65 (3), 227–248. doi: 10.1016/s0034-4257(98)00064-9

Guarini, R., Loizzo, R., Facchinetti, C., Longo, F., Ponticelli, B., Faraci, M., et al. (2018). "PRISMA hyperspectral mission products," in *IGARSS 2018-2018 IEEE International Geoscience and Remote Sensing Symposium* (IEEE), 179–182.

Habermeyer, M., Baumann, S., Carmona, E., Chabrillat, S., Krieger, V., La Porta, L., et al. (2024). "EnMAP operations in light of data product statistics," in *2024 14th Workshop on Hyperspectral Imaging and Signal Processing: Evolution in Remote Sensing (WHISPERS)* (IEEE), 1–5.

Hadjal, M., Medina-Lopez, E., Ren, J., Gallego, A., and McKee, D. (2022). An artificial neural network algorithm to retrieve chlorophyll a for northwest European shelf seas from top of atmosphere ocean colour reflectance. *Remote Sensing* 14 (14), 3353. doi: 10.3390/rs14143353

Hoffer, Ro M., and Chris, J. J. (1969). "Ecological potentials in spectral signature analysis," in *Remote Sensing in Ecology*, 1–16.

Im, J., and Jensen, J. R. (2008). Hyperspectral remote sensing of vegetation. *Geogr. Compass* 2 (6), 1943–1961. doi: 10.1111/j.1749-8198.2008.00182.x

Italian Space Agency (2024). *PRISMA General Conditions for the Provision of Products, License and Project Form to Be Compiled by the User*. Available online at: https://prismauserregistration.asi.it/LICENCE_TO_USE_PRISMA_DATA.pdf (accessed on 25 February 2025).

Iwasaki, A., Ohgi, N., Tanii, J., Kawashima, T., and Inada, H. (2011). "Hyperspectral imager suite (HISUI)-japanese hyper-multi spectral radiometer," in *2011 IEEE International Geoscience and Remote Sensing Symposium* (IEEE), 1025–1028.

Kaufmann, H., Segl, K., Chabrillat, S., Müller, A., Richter, R., Schreier, G., et al. (2005). "EnMAP–An advanced hyperspectral mission," in *Proceedings of 4th Earsel Workshop on Imaging Spectroscopy (Warsaw 2005)*, 55–60.

Kruse, F. A., Boardman, J. W., Lefkoff, A. B., Young, J. M., Kierein-Young, K. S., Cocks, T. D., et al. (2000). "HyMap: an Australian hyperspectral sensor solving global problems-results from USA HyMap data acquisitions," in *Proc. of the 10th Australasian Remote Sensing and Photogrammetry Conference*, 18–23.

Krutz, D., Müller, R., Knodt, U., Günther, B., Walter, I., Sebastian, I., et al. (2019). The instrument design of the DLR earth sensing imaging spectrometer (DESIS). *Sensors* 19 (7), 1622. doi: 10.3390/s19071622

Lamelas-Gracia, M. T., Riaño, D., and Ustin, S. (2019). A LiDAR signature library simulated from 3-dimensional discrete anisotropic radiative transfer (DART) model to classify fuel types using spectral matching algorithms. *GIScience and Remote Sens.* 56 (7), 988–1023. doi: 10.1080/15481603.2019.1601805

Leitão, P. J., Schwieder, M., Suess, S., Okujeni, A., Galvão, L. S., Linden, S. V. D., et al. (2015). Monitoring natural ecosystem and ecological gradients: perspectives with EnMAP. *Remote Sens.* 7 (10), 13098–13119. doi: 10.3390/rs71013098

Liu, Y. N., Sun, D. X., Hu, X. N., Ye, X., Li, Y. D., Liu, S. F., et al. (2019). The advanced hyperspectral imager: aboard China's GaoFen-5 satellite. *IEEE Geoscience Remote Sens. Mag.* 7 (4), 23–32. doi: 10.1109/mgrs.2019.2927687

Liu, C., Hu, Q., Zhang, C., Xia, C., Yin, H., Su, W., et al. (2022). First Chinese ultraviolet–visible hyperspectral satellite instrument implicating global air quality during the COVID-19 pandemic in early 2020. *Light Sci. and Appl.* 11 (1), 28. doi: 10.1038/s41377-022-00722-x

Loizzo, R., Guarini, R., Longo, F., Scopa, T., Formaro, R., Facchinetti, C., et al. (2018). "PRISMA: the Italian hyperspectral mission," in *IGARSS 2018-2018 IEEE International Geoscience and Remote Sensing Symposium* (IEEE), 175–178.

Mahalingam, S., Srinivas, P., Devi, P. K., Sita, D., Das, S. K., Leela, T. S., et al. (2019). "Reflectance based vicarious calibration of HySIS sensors and spectral stability study over pseudo-invariant sites," in *2019 IEEE Recent Advances in Geoscience and Remote Sensing: Technologies, Standards and Applications (TENGARSS)* (IEEE), 132–136.

Manago, N., Takara, Y., Ando, F., Noro, N., Suzuki, M., Irie, H., et al. (2018). Visualizing spatial distribution of atmospheric nitrogen dioxide by means of hyperspectral imaging. *Appl. Opt.* 57 (21), 5970–5977. doi: 10.1364/AO.57.005970

Martinez, M. N., and Bartholomew, M. J. (2017). What does it "mean"? A review of interpreting and calculating different types of means and standard deviations. *Pharmaceutics* 9 (2), 14. doi: 10.3390/pharmaceutics9020014

Mobley, C. D. (1999). Estimation of the remote-sensing reflectance from above-surface measurements. *Appl. Optics* 38 (36), 7442–7455. doi: 10.1364/ao.38.007442

Musacchio, M., Silvestri, M., Romaniello, V., Casu, M., Buongiorno, M. F., and Melis, M. T. (2024). Comparison of ASI-PRISMA data, DLR-EnMAP data, and field spectrometer measurements on "Sale 'e Porcus". *A Salty Pond Sard. Italy. Remote Sens.* 16 (6), 1092. doi: 10.3390/rs16061092

Nieke, J., Despoisse, L., Gabriele, A., Weber, H., Strese, H., Ghasemi, N., et al. (2023). The copernicus hyperspectral imaging mission for the environment (CHIME): an overview of its mission, system and planning status. *Sensors, Syst. Next-Generation Satell. XXVII* 12729, 21–40. doi: 10.1117/12.2679977

Palmer, P. I., Jacob, D. J., Chance, K., Martin, R. V., Spurr, R. J., Kurosu, T. P., et al. (2001). Air mass factor formulation for spectroscopic measurements from satellites: application to formaldehyde retrievals from the global ozone monitoring experiment. *J. Geophys. Res. Atmos.* 106 (D13), 14539–14550. doi: 10.1029/2000jd900772

Pascual-Venteo, A. B., Garcia, J. L., Berger, K., Estévez, J., Vicent, J., Pérez-Suay, A., et al. (2024). Gaussian process regression hybrid models for the top-of-atmosphere retrieval of vegetation traits applied to PRISMA and EnMAP imagery. *Remote Sens.* 16 (7), 1211. doi: 10.3390/rs16071211

Pearlman, J. S., Barry, P. S., Segal, C. C., Shepanski, J., Beiso, D., and Carman, S. L. (2003). Hyperion, a space-based imaging spectrometer. *IEEE Trans. Geoscience Remote Sens.* 41 (6), 1160–1173. doi: 10.1109/tgrs.2003.815018

Plajer, I. C., Băicoianu, A., Majercsik, L., and Ivanovici, M. (2023). "Ndvi computation from hyperspectral images," in *2023 13th Workshop on Hyperspectral Imaging and Signal Processing: Evolution in Remote Sensing (WHISPERS)* (IEEE), 1–5.

Qian, S. E. (2022). "Overview of hyperspectral imaging remote sensing from satellites," in *Advances in Hyperspectral Image Processing Techniques*, 41–66.

Rajabi, R., Zehtabian, A., Singh, K. D., Tabatabaeenejad, A., Ghamisi, P., and Homayouni, S. (2024). Hyperspectral imaging in environmental monitoring and analysis. *Front. Environ. Sci.* 11, 1353447. doi: 10.3389/fenvs.2023.1353447

Rasooli, N., Mirzaei, S., and Pignatti, S. (2024). *Prospective Case Study of Gypsum Retrieval in Agricultural Soil by Advanced Spaceborne Hyperspectral Imagers (Prisma and Enmap) in Sirjan Playa*. Central Iran. Central Iran.

Saberioon, M., Khosravi, V., Brom, J., Gholizadeh, A., and Segl, K. (2023). Examining the sensitivity of simulated EnMAP data for estimating chlorophyll-a and total suspended solids in inland waters. *Ecol. Informatics* 75, 102058. doi: 10.1016/j.ecoinf.2023.102058

Schaepman, M. E., Jehle, M., Hueni, A., D'Odorico, P., Damm, A., Weyermann, J., et al. (2015). Advanced radiometry measurements and Earth science applications with the airborne prism experiment (APEX). *Remote Sens. Environ.* 158, 207–219. doi: 10.1016/j.rse.2014.11.014

Schaepman-Strub, G., Schaepman, M. E., Painter, T. H., Dangel, S., and Martonchik, J. V. (2006). Reflectance quantities in optical remote sensing—Definitions and case studies. *Remote Sensing Environment* 103 (1), 27–42. doi: 10.1016/j.rse.2006.03.002

Stuart, M. B., McGonigle, A. J., and Willmott, J. R. (2019). Hyperspectral imaging in environmental monitoring: a review of recent developments and technological advances in compact field deployable systems. *Sensors* 19 (14), 3071. doi: 10.3390/s19143071

Stuffler, T., Förster, K., Hofer, S., Leipold, M., Sang, B., Kaufmann, H., et al. (2009). Hyperspectral imaging—An advanced instrument concept for the EnMAP mission (environmental mapping and analysis programme). *Acta Astronaut.* 65 (7-8), 1107–1112. doi: 10.1016/j.actaastro.2009.03.042

The German Aerospace Center (2025). EnMAP – License agreement on the use of EnMAP data. Available online at: https://www.enmap.org/data/resources/EnMAP_Data_License.pdf (accessed on February 25, 2025).

Thuillier, G., Hersé, M., Labs, D., Foujols, T., Peetermans, W., Gillotay, D., et al. (2003). The solar spectral irradiance from 200 to 2400 nm as measured by the SOLSPEC spectrometer from the atlas and eureca missions. *Sol. Phys.* 214, 1–22. doi: 10.1023/a:1024048429145

Xue, Y., Kuze, H., Chen, W., Kaneta, S., Takamura, T., and Takeuchi, N. (2000). Simultaneous observation of NO2 column density and aerosol optical thickness in urban atmosphere. *Opt. Review* 7 (1), 89–94. doi: 10.1007/s10043-000-0089-7

Yang, C., Everitt, J. H., and Bradford, J. M. (2008). Yield estimation from hyperspectral imagery using spectral angle mapper (SAM). *Trans. ASABE* 51 (2), 729–737. doi: 10.13031/2013.24370

Zandler, H., Brenning, A., and Samimi, C. (2015). Potential of space-borne hyperspectral data for biomass quantification in an arid environment: advantages and limitations. *Remote Sens.* 7 (4), 4565–4580. doi: 10.3390/rs70404565

Zdravcheva, N. D. (2019). Hyperspectral environmental monitoring. In IOP conference series: materials science and engineering. *IOP Publ.* 614 (1), 012014. doi: 10.1088/1757-899X/614/1/012014

Zscheile, F. P., and Comar, C. L. (1941). Influence of preparative procedure on the purity of chlorophyll components as shown by absorption spectra. *Bot. Gaz.* 102 (3), 463–481. doi: 10.1086/334981

Glossary

AMF	Air Mass Factor
AMF_G	Geometric Air Mass Factor
APEX	Airborne Prism Experiment
ASI	Italian Space Agency
AVIRIS	Airborne Visible/Infrared Imaging Spectrometer
BOA	Bottom of Atmosphere
BRDF	Bidirectional Reflectance Distribution Function
CASI	Compact Airborne Spectrographic Imager
CH_4	Methane
CHEOS	China High-resolution Earth Observation System
CHL	Chlorophyll
DESIS	DLR Earth Sensing Imaging Spectrometer
DLR	German Aerospace Center
EMIT	Earth surface Mineral dust source InvesTigation
EnMAP	Environmental Mapping and Analysis Program
ESA	European Space Agency
FWHM	Full Width at Half Maximum
GF-5	Gaofen 5
GSD	Ground Sampling Distance
HISUI	Hyperspectral Imager Suite
HyMap	Hyperspectral Mapper
HySIS	Hyper Spectral Imaging Spectrometer
ISRF	Instrumental Spectral Response Function
ISRO	Indian Space Research Organisation
JPL	Jet Propulsion Laboratory
MDPI	Multidisciplinary Digital Publishing Institute
METI	Japanese Ministry of Economy, Trade, and Industry
MODTRAN	MODerate resolution atmospheric TRANsmission
NASA	National Aeronautics and Space Administration
NDVI	Normalized Difference Vegetation Index
NO_2	Nitrogen Dioxide
PRISMA	PRecursore IperSpettrale della Missione Applicativa
RMSE	Root Mean Square Error
SAM	Spectral Angle Mapper
STD	Standard Deviation
SWIR	Short Wave InfraRed
SZA	Solar Zenith Angle
TOA	Top of Atmosphere
VIS	Visible
VNIR	Visible and Near InfraRed
VZA	Viewing Zenith Angle